Mathematics and Systems Science 2025, 3(1), 3108.
https://doi.org/10.54517/mss3108

Article

Receptivity of flow in a square lid driven cavity to implicit numerical excitations for high-fidelity HPC

Tapan K. Sengupta[1,*], Abhinav Prakash[2], Aditi Sengupta[2], Suman K. Vajjala[3]

[1] High Performance Computing Laboratory, IIT, Kanpur 208016, India
[2] Dept. of Mechanical Engineering IIT(ISM), Dhanbad 826004, India
[3] CTFD Division, National Aerospace Laboratories, Bangalore 560017, India
*** Corresponding author:** Tapan K. Sengupta, tksen@iitk.ac.in

CITATION

Sengupta TK, Prakash A, Sengupta A, Vajjala SK. Receptivity of flow in a square lid driven cavity to implicit numerical excitations for high-fidelity HPC. Mathematics and Systems Science. 2025; 3(1): 3108. https://doi.org/10.54517/mss3108

ARTICLE INFO

Received: 28 November 2024
Accepted: 13 February 2025
Available online: 27 February 2025

Abstract: This study aims to investigate the effects of implicit numerical excitation on the receptivity of flow inside a square lid-driven cavity (LDC) leading to bifurcation and instability for a fixed (257 × 257) grid with different temporal resolutions via the solution of the Navier-Stokes equation. Computational results have been provided showing the flow dynamics of the LDC problem as explained with a time series at a representative point near the top corner of the cavity at (0.95, 0.95) for supercritical Reynolds numbers with respect to the bifurcation phenomenon by lowering the time step. As the accuracy of numerical methods plays a vital role in capturing the dynamics at different Reynolds numbers, this vortex-dominated flow is explained for bifurcation and instability. We propose this as a benchmark problem for the direct numerical simulation (DNS) and for machine learning (ML) of fluid flow that will lead to efficient ML algorithms and an understanding of flow receptivity, instability, and transition by DNS.

Keywords: lid-driven cavity flow; direct numerical simulation; high-performance computing; bifurcation analysis; receptivity analysis; global spectral analysis; error dynamics; machine learning of flows

1. Introduction

Flow inside a lid-driven cavity (LDC) is considered a classical non-periodic problem among researchers in scientific computing because of its unique boundary conditions, which allow one to test the accuracy of the numerical method for solving the Navier-Stokes equation (NSE). It also aids in comprehending the nonlinear dynamics of vortex-driven unsteady flows, which will set a benchmark problem for quantifying direct numerical simulation (DNS) and testing machine learning purposes. As shown in the schematic of the problem in **Figure 1**, the top lid is subjected to a constant translational velocity (U) that provides the Reynolds numbers ($Re = U\nu/L$, where ν represents the kinematic viscosity, and L is the side of the square LDC). The flow inside the LDC becomes unsteady due to the growth of disturbances, as created by omnipresent numerical errors and other epistemic errors like aliasing errors. The unavoidable numerical errors due to round-off and dispersion errors make the flow inherently unsteady above a critical Reynolds number (Re_{cr}); precise knowledge of the same eluded us before. Numerous two-dimensional (2D) studies have been reported using the most accurate vorticity-stream function formulation of the incompressible NSE. A typical representative work using a coupled strongly implicit multigrid method to obtain the solutions for Re up to 10,000 with (257 × 257) and (129 × 129) grids has been reported in Ghia et al. [1]. However, a steady-state solution was

achieved for Re = 10,000, for which no reason was provided, and this discrepancy is explained here for the first time. This is related to the acquired knowledge by global spectral analysis (GSA) of numerical methods in Sengupta et al. [2], Sagaut et al. [3], Sengupta [4] and Sengupta et al. [5], which enabled to develop extremely high accuracy and dispersion relation preserving combined compact difference (CCD) schemes, as in Sengupta et al. [6] and in Ozbenli and Vedula [7]. A highly accurate new combined compact difference (NCCD) scheme was implemented to calculate the first and second derivatives simultaneously to improve the original CCD scheme. With the NCCD method, the usual sources of error due to discretization are minimized, while unsteadiness arises at higher Reynolds numbers due to aliasing error, Gibbs' phenomenon (described in Sengupta et al. [8]), with the latter being due to the physical discontinuity of the velocity boundary condition at the ends of the top lid. In consequence, the corner points have zero vorticity, while adjacent points exhibit high wall vorticity. This discrete change between the corner and neighboring points results in Gibbs' phenomenon at the top corners. This has been identified at the corners of the top lid in the pseudo-spectral computation of the NSE in Auteri et al. [9] and in Botella and Peyret [10]. The aliasing errors are distributed at all the points of the top lid, as explained in Suman et al. [11]. Steady flow in LDC analyzed and computed in Burgraff [12], however, displays unsteadiness at varying Re values, as described in Schreiber and Keller [13]. For higher Re, the LDC flow experiences solution bifurcation by various sources of numerical errors to display unsteadiness, as have been described in Lestandi et al. [14]. Schreiber and Keller [13] reported a solution for Re = 10,000 on a (180 × 180) grid, adapting a Newton-like method useful for nonlinear systems.

High accuracy results presented for Re = 10,000 in Sengupta et al. [6] using a (257 × 257) grid indicated the creation of a transient polygonal vortex at the core with permanent gyrating satellite vortices around the core. These results were obtained using sequential computing. Solving such high-Re LDC flow accurately using parallel computing is not trivial. This was shown for the first time in Suman et al. [11], with results obtained using (1025 × 1025) and (2049 × 2049) grids by the non-overlapping high accuracy parallel (NOHAP) scheme reported in Sengupta et al. [15] and Sundaram et al. [16]. This special scheme was developed to remove any errors at the subdomain boundaries when overlapping parallel compact schemes were used. Earlier sequential computing methods have been used to obtain the first Re_{cr}, as reported by different numerical methods in Lestandi et al. [14]. It also demonstrated that for high Re, following the first Hopf bifurcation, the flow in the limit cycle suffers a secondary instability requiring a significantly longer computing time, which earlier studies on the topic did not practice. In the presented results, we report results obtained with very high accuracy HPC simulated over very long times.

A machine-learning-based solver for NSE using finite volume discretization has been described in Ranade et al. [17]. In Sahin and Owens [18], the implicit finite volume method was used for this flow by removing the pressure term from the momentum equation and multiplying it with the unit normal vector to control the volume boundary and afterward integrating from that boundary. Using a second-order spectral projection method, the Re_{cr} within an interval was pinpointed in the interval (8017.6, 8018.8) in Auteri et al. [9]. Sahin and Owens [18] reported the critical Reynolds number to be 8031.93. Bruneau and Saad [19] identified this range as

between 8000 and 8050, though they did not present any bifurcation diagram. Their analysis used a (1024 × 1024) grid with third- and fifth-order spatial discretization schemes. However, use of the three-time-level Gear method introduced an artificial mode, which impacted the overall accuracy of the results in Bruneau and Saad [19]. Regularizing the lid's velocity at the ends can reduce the discontinuous velocity (eliminating Gibbs' phenomenon), but it cannot eliminate aliasing error.

A vorticity time series plot shown in Lestandi et al. [14], indicates initial temporal growth followed by nonlinear saturation. Multiple Hopf bifurcations with varying *Re* for both excited and unexcited cases were shown for (257 × 257) and (513 × 513) grids in this reference [14]. Parallel computing results for the finer grids with (1025 × 1025) and (2049 × 2049) points in Suman et al. [11], also showed a pentagonal vortex at the center, which eventually morphed into a triangular vortex. Experimental demonstration of polygonal vortices have been reported by Beckers and van Heijst [20], Carnevale and Kloosterziel [21] and Jansson et al. [22]. In the presented results by sequential and parallel computations of the governing vorticity transport equation, one observes such polygonal vortices in the vorticity contours. To solve the stream function equation, the Bi-CGSTAB method of Van der Vorst [23] is employed.

The effect of various errors due to aliasing and Gibbs' phenomenon causing discontinuous jumps at corners for finer grids was explained in Suman et al. [11]. It was also observed that by regularizing corner singularities, the critical Reynolds number Re_{cr1} could be extended in the range of (10,000–10,500). DNS reveals spatiotemporal disturbance growth and nonlinear saturation, distinguishing it from classical bifurcation studies that limit the analysis to temporal instability only, as in Landau and Lifshitz [24]. Effects of varying spatial resolution in the 2D LDC were investigated by explicitly exciting the flow at varying amplitudes and frequencies in Suman et al. [11].

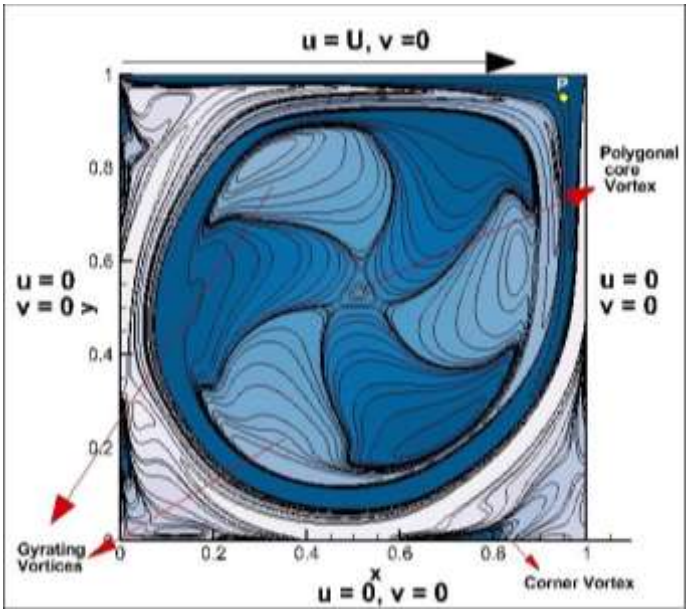

Figure 1. The schematic of the problem with sample point P is located at (0.95, 0.95) in the computational domain for (257 × 257) grid points.

In the presented results here, the same NOHAP scheme developed in Sengupta et al. [15] and in Sundaram et al. [16] has been adopted with parallelization imposed in the *x*-direction only. The main emphasis here is to obtain the Re_{cr} value as accurately as possible, i.e., dictated by GSA in Sagaut et al. [3], Sengupta [4] and Sengupta et al. [5] with the relative dominant roles of the Courant-Friedrichs-Lewy (CFL) and the diffusion numbers. It is essential to note that this internal flow is diffusion-dominated and not convection-dominated. One of the principal goals of the present research is to create a benchmark set of results that can be used in studies of artificial intelligence and machine learning in fluid mechanics, as in Brunton et al. [25], Jiang et al. [26], Amalmadhi et al. [27] and McDevitt et al. [28].

Unlike early simulations of LDC flows by sequential computing, high-performance computing was carried out with (257 × 257), (513 × 513), and (1025 × 1025) grid points in Suman et al. [11], using explicit excitation for parallel computing using NOHAP closure developed in Sengupta et al. [15] and Sundaram et al. [16]. Present research builds on this HPC approach to perform receptivity analysis, as given in Sengupta [29], by implicitly exciting the flow through initial excitation by varying temporal resolutions to show the importance of diffusion over convection for the LDC flow. This is a novel approach for this study to provide DNS results with extreme accuracy. Such high accuracy, high-performance calculation enables one to compute transitional and turbulent flows, capturing the underlying physics of the receptivity approach, and those results create the benchmark for DNS, reduced-order models, and databases for machine learning.

The paper is formatted in the following manner: In Section 2, the governing equation and the numerical methods used are described briefly. In Section 3, the vorticity dynamics of the LDC flow are described for a representative supercritical *Re* = 8500. The multiple Hopf bifurcation is noted for flows at different *R*e in Section 4. In subsection 4.1, a brief description of GSA is provided using the convection-diffusion equation. The onset of instability is described in section 5. The paper closes with a summary and conclusions.

2. Governing equation and numerical method adapted

A DNS for 2D square LDC flow is performed using the stream function-vorticity formulation of the NSE. The governing stream function equation and the vorticity transport equation are as given in the following:

$$\nabla^2\psi = -\omega \tag{1}$$

$$\frac{\partial\omega}{\partial t} + \left(\vec{V}.\nabla\right)\omega = \frac{1}{Re}\nabla^2\omega \tag{2}$$

where ω is the nonzero component of vorticity normal to the flow for the proposed 2D square LDC problem. The velocity vector is defined as $\vec{V} = \nabla \times \vec{\Psi}$, where $\vec{\Psi}$ = $[0,0,\psi]$. Non-dimensionalization of NSE was done using *L* and *U* as corresponding length and velocity scales, respectively. The following boundary conditions are imposed to solve Equations (1) and (2). The stream function ψ is held constant on all four cavity walls, enforcing the no-slip condition. The wall vorticity ω_b is precisely

defined by $\omega_b = -\frac{\partial^2\psi}{\partial n^2}$, where n is the wall-normal coordinate selected for each cavity wall. Using Taylor series expansion at the wall, ω_b is calculated with velocity boundary conditions specified along each segment. To solve the discretized form of Equation (1), the Bi-CGSTAB method of Van der Vorst [23], a fast and convergent solver for elliptic partial differential equations, is employed. The convection and diffusion terms in Equation (2) are discretized with the NCCD method in Sengupta et al. [6], enabling the simultaneous computation of both first and second-order derivatives. The stencil of the NCCD scheme for computing derivatives is given below in brief, with a single prime indicating a first derivative and a double prime indicating a second derivative. Further details on CCD and related compact schemes are available in Sengupta [4].

$$u_1' = \frac{1}{2h}[-3u_1 + 4u_2 - u_3]$$

$$u_1'' = \frac{1}{h^2}[u_1 - 2u_2 + u_3]$$

$$u_2' = \frac{1}{h}[(\frac{2\beta}{3} - \frac{1}{3})u_1 - (\frac{8\beta}{3} + \frac{1}{2})u_2 + (4\beta + 1)u_3 - (\frac{8\beta}{3} + \frac{1}{6})u_4 + \frac{2\beta}{3}u_5]$$

$$u_2'' = \frac{1}{h^2}[u_1 - 2u_2 + u_3]$$

$$\frac{7}{16}(u_{j+1}' + u_{j-1}') + u_j' - \frac{h}{16}(u_{j+1}'' - u_{j-1}'') = \frac{15}{16h}(u_{j+1} - u_{j-1}), j = 3,\cdots,N-2$$

$$\frac{9}{8h}(u_{j+1}' + u_{j-1}') - \frac{1}{8}(u_{j+1}'' - u_{j-1}'') + u_j'' = \frac{3}{h^2}(u_{j+1} - 2u_j + u_{j-1}), j = 3,\cdots,N-2$$

$$u_{N-1}' = \frac{-1}{h}[(\frac{2\beta}{3} - \frac{1}{3})u_N - (\frac{8\beta}{3} + \frac{1}{2})u_{N-1} + (4\beta + 1)u_{N-2} - (\frac{8\beta}{3} + \frac{1}{6})u_{N-3} + \frac{2\beta}{3}u_{N-4}]$$

$$u_{N-1}'' = \frac{1}{h^2}[u_N - 2u_{N-1} + u_{N-2}]$$

$$u_N' = \frac{1}{2h}[3u_N - 4u_{N-1} + u_{N-2}]$$

$$u_N'' = \frac{1}{h^2}[u_N - 2u_{N-1} + u_{N-2}]$$

$$\beta = -0.025 \text{ for } j = 2 \text{ and } \beta = 0.09 \text{ for } j = N-1 \tag{3}$$

The system of Equations (3) is solved using a block tridiagonal matrix algorithm (TDMA) to obtain the derivatives. These derivatives (in both directions for the two-dimensional problems) are needed in solving both the stream function equation and the vorticity transport equation.

To advance Equation (2) in time, a four-stage, fourth-order Runge-Kutta (RK_4) method is utilized, whose algorithm is given below.

$$u^{(1)} = u^{(n)} + \frac{\Delta t}{2}L(u^{(n)})$$

$$u^{(2)} = u^{(n)} + \frac{\Delta t}{2} L(u^{(1)})$$

$$u^{(3)} = u^{(n)} + \Delta t L(u^{(2)})$$

$$u^{(n+1)} = u^{(n)} + \frac{\Delta t}{6}[L(u^{(n)}) + 2L(u^{(1)}) + 2L(u^{(2)}) + L(u^{(3)}) \quad (4)$$

where the governing equation is expressed in the form $\frac{\partial u}{\partial t} = L(u)$, and the superscripts denote the stages of the RK scheme. These simulations are highly sensitive to the numerical properties given by the GSA.

Parallelizing the code using the Schwarz domain decomposition technique fails to reproduce the results from sequential computation despite many overlapping points being used at the subdomain boundaries, as explained in Sengupta et al. [15] and Sundaram et al. [16]. Here, a parallelization approach that circumvents the need for overlapping subdomains while preserving the accuracy of the sequential NCCD method is used. The parallel algorithm follows a strategy of preserving the accuracy of the compact scheme used in the interior by completely eliminating errors caused by subdomain closure. The parallelization process has been applied in two phases: in the first phase, the compact scheme, which is used in the interior, has been pre-conditioned to allocate the essential information for computing the first derivatives at an interior point. This information is subsequently used at the boundary stencils for the subdomain boundaries, with the details given in Sengupta et al. [15] and Sundaram et al. [16].

3. Flow dynamics of square LDC for $Re = 8500$ and $\Delta t = 5 \times 10^{-5}$

Computational results for vorticity inside the LDC for Re = 8500 have been shown in **Figure 2** at the point P, whose coordinate is given as (0.95, 0.95), and the computational results are obtained with the time step of $\Delta t = 5 \times 10^{-5}$ and a uniform (257 × 257)-grid. From the vorticity time series shown in the middle, we can observe that the flow shows a massive transient initially that takes time to settle down to a steady state subsequently. It is observed that from non-dimensional time t = 400, where the flow is steady, one can see coherent circular vortices at the core. At the onset of instability, the amplitude of vorticity increases exponentially during the initial growth up to about t = 595, beyond which the core morphs into a triangular shape. At time t = 650, the outer layer transforms into gyrating satellite vortices; at this instant, the core is perfectly transformed into a triangular shape. Such a triangular core shape has been reported earlier only in Sengupta et al. [6]. Thereafter, in the limit cycle oscillation region, i.e., when nonlinearity prevails with the growth of vorticity saturates, as noted at t = 850, we can observe the core vortex to start shrinking. Then, the flow is guided by six gyrating satellite vortices alternating in sign. Experimental evidences in Beckers and van Heijst [20], Carnevale and Kloosterzeil [21] and Jansson et al. [22], derived from dye visualization techniques in rotating flows, demonstrated the physical presence of triangular vortices. Capturing such a triangular vortex at the center of the LDC necessitates accurate spatial and temporal discretization. In computational

analyses, it is necessary that a highly accurate numerical method minimize different sources of errors and successfully capture the polygonal core vortices.

However, any inaccuracies in modeling and/or adding spurious dissipation and dispersion hinder capturing such core vortices. One notes that complex interactions of vortices forming inside the LDC highlight the dynamics and nature of flow patterns within the cavity.

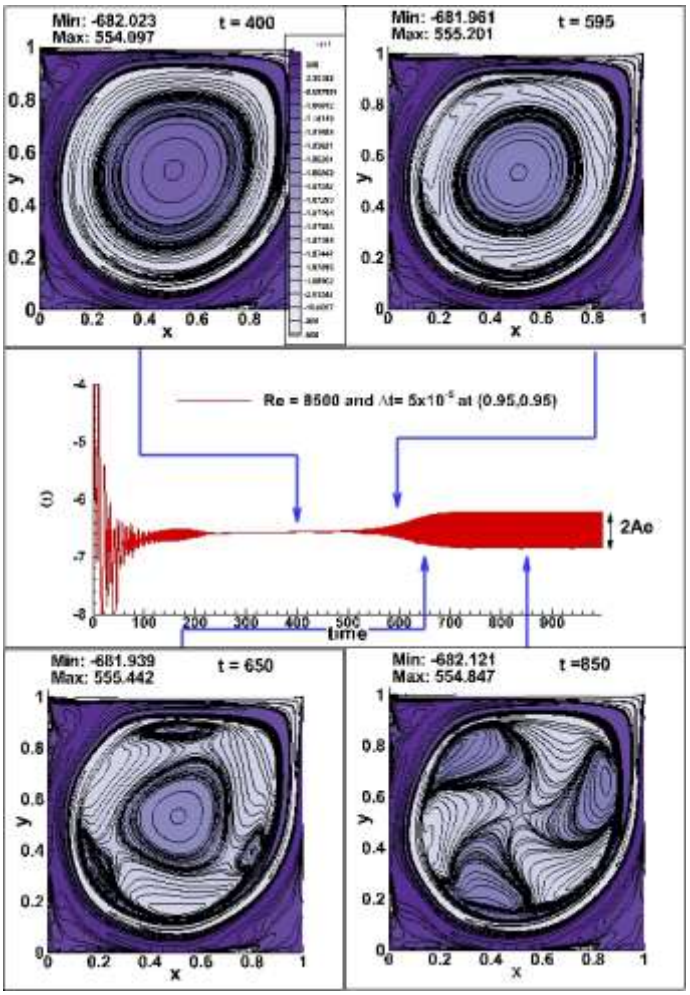

Figure 2. Time series for *Re* = 8500 at the timestep $\Delta t = 5 \times 10^{-5}$ at the sample point P, along with vorticity contours plotted at different times.

4. Multiple Hopf bifurcation analysis

As observed from the vorticity time series in **Figure 2** at P (0.95, 0.95), the flow undergoes temporal linear instability to begin with. Subsequently, at a later time, nonlinearity becomes significant, causing the growth to saturate and the amplitude to stabilize, forming a limit cycle while reaching a new equilibrium amplitude A_e, as illustrated in **Figure 2**. The Stuart-Landau-Eckhaus equation, as has been progressively developed in Landau and Lifshtiz [24], Drazin and Reid [30], Ekhaus [31] and Sengupta et al. [32], that effectively explains this phenomenon by expanding the eigenfunctions, as in Ekhaus [31], Sengupta et al. [32] using the Galerkin method for proper orthogonal decomposition (POD). The Stuart-Landau equation was formulated originally under the assumption of a single unstable modal growth in

Landau and Lifshitz [24]. In contrast, in the present case, it is observed that the flow inside the cavity exhibits distinct multimodal characteristics. To address this issue, Eckhaus proposed more general equations that accounted for nonlinear interactions between different combinations of modes, including self-interactions in Ekhaus [31] and Sengupta et al. [32].

Originally, Landau proposed a relationship between the equilibrium amplitude (A_e) and *Re* as, $A_e^2 \propto (Re - Re_{cr1})$ for flow attaining a limit cycle by considering a single mode only. Lestandi et al. [14] plotted A_e versus *Re* curve, where Hopf bifurcation was reported to start between *Re* = 8600 and 8670 for a (257 × 257) grid size used with the NCCD scheme for a sequential code. Discontinuity was seen in the curve, indicating the presence of multiple Hopf bifurcations. Following these observations, studies were carried out in Suman et al. [11], showing the same A_e versus *Re* plot for grids with (257 × 257), (513 × 513), and (1025 × 1025) points, by using explicit excitation for parallel computing using NOHAP closure. The present research builds on previous ones and presents a receptivity analysis for the LDC flow. This is achieved by implicitly exciting the flow by different excitations associated with numerical sources of errors with varying temporal resolutions, unlike explicit excitation in Suman et al. [11]. The bifurcation diagram shown in **Figure 3** for two time steps of $\Delta t = 5 \times 10^{-5}$ and $\Delta t = 2 \times 10^{-5}$ provides insight into how the flow behavior changes for different temporal resolutions that determine the level of numerical error to trigger the receptivity of the flow field. The red line indicates the higher time step that shows a slope discontinuity of the curve at *Re* = 8600 with a kink, which is clear evidence of multiple Hopf bifurcations present, as explained in Sengupta et al. [32].

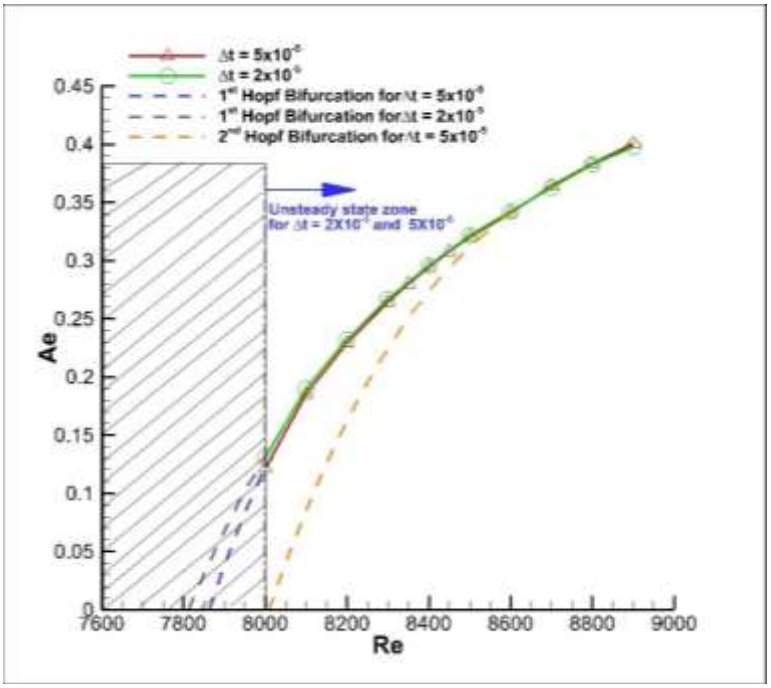

Figure 3. Equilibrium amplitude (A_e) as a function of *Re* is shown in the bifurcation diagram for the time steps of $\Delta t = 5 \times 10^{-5}$ and $\Delta t = 2 \times 10^{-5}$.

For the chosen two time steps, simulations are performed for Reynolds numbers above and equal to 8000, for which terminal unsteady flows have been obtained. This is indicated by the vertical line for *Re* = 8000, above which the LDC flow is definitely unsteady. The hatched area to the left of this vertical line has been investigated, with cases having been computed extensively for long times without showing unsteadiness for these two time steps. Simulations at such lower Reynolds numbers can be performed for smaller time steps and for longer durations for exact estimation of critical *Re*.

It has also been observed that for *Re* = 8000, one gets an unsteady solution for $\Delta t = 5 \times 10^{-5}$ at a significantly later time, while an unsteady solution is obtained for $\Delta t = 2 \times 10^{-5}$ much earlier, as shown in **Figure 4** with the help of the displayed time series. This type of flow receptivity has never been reported in the literature before.

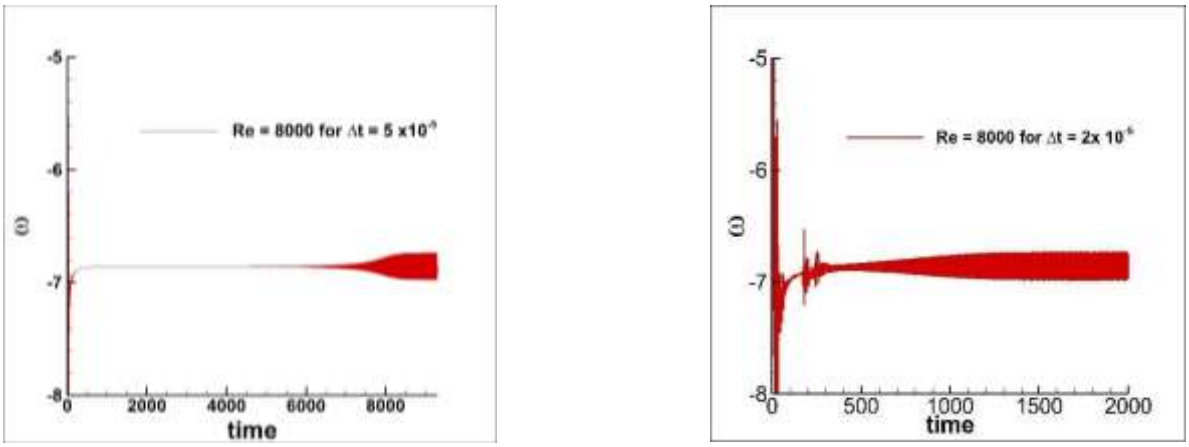

(a) **(b)**

Figure 4. Time series for *Re* 8000 for time steps **(a)** $\Delta t = 5 \times 10^{-5}$ (shown till $t = 9297$); and **(b)** $\Delta t = 2 \times 10^{-5}$ (shown till $t = 2148$).

Global spectral analysis for convection-diffusion equation

To explain the physics of LDC flow governed by NSE for post-critical Reynolds number, the GSA is performed for the model 1D convection-diffusion equation that models the feature of the NSE solved here by using RK_4 for the time advancement strategy and the NCCD scheme used for spatial discretization. Such an analysis helps one to choose grid spacings, time steps, and other numerical parameters so that the simulation provides the high fidelity required for DNS and its application in machine learning.

The 1D convection-diffusion equation can be represented as:

$$\frac{\partial u}{\partial t} + c\frac{\partial u}{\partial x} = \alpha\frac{\partial^2 u}{\partial x^2} \tag{5}$$

where c and α are the constant phase speed and the diffusion coefficient, respectively. To perform GSA, we transform the unknown u from the physical to the spectral plane as introduced in Sengupta et al. [2], Sagaut et al. [3] and Sengupta [4],

$$u(x,t) = \int \hat{U}(k,t)e^{ikx}\,dk \tag{6}$$

where $\widehat{U}$ represents the Fourier amplitude; k represents the wavenumber and the integral is performed over the Bromwich contours in the spectral plane, as given in Sengupta [29,33]. After substituting the expression of u from Equation (6) in Equation (5), one obtains,

$$\frac{d\widehat{U}}{dt} + ick\widehat{U} = -\alpha k^2 \widehat{U} \tag{7}$$

The above ordinary differential equation, Equation (7), is solved by taking a general initial condition $u(x,0) = f(x) = \int \hat{F}(k)e^{ikx}dk$ to obtain the solution as,

$$u(x,t) = \int \hat{F}\,(k)e^{-\alpha k^2 t}e^{-ikct} \tag{8}$$

We have the physical dispersion relation by taking the unknown $u(x,t)$ and doing its bi-dimensional Fourier-Laplace transform. We can write:

$$u(x,t) = \iint \widehat{U}(k,\omega)e^{i(kx-\omega t)}dkd\omega \tag{9}$$

where the integrals are again performed along the Bromwich contours in the wavenumber and circular frequency planes, as explained in Sengupta [29,33]. Substituting the above expression in Equation (5), the physical dispersion relation is finally obtained as,

$$\omega = ck - i\alpha k^2 \tag{10}$$

The phase speed is obtained from the dispersion relation expressed as,

$$c_{\text{phys}} = \frac{\omega}{k} = c - i\alpha k \tag{11}$$

The physical group velocity is therefore defined as,

$$V_{g,\text{phys}} = \frac{\partial \omega}{\partial k} = c - 2i\alpha k \tag{12}$$

The role of complex group velocity and energy propagation speed is discussed in detail in Sengupta et al. [2] and Sagaut et al. [3]. By expanding the real and imaginary parts of Equation (12), we get:

$$\alpha = \frac{i}{2k}\left[\left(V_{g,\text{phys}}\right)_{\text{real}} - c\right] - \frac{(V_{g,\text{phys}})_{\text{imag}}}{2k} \tag{13}$$

The physical amplification factor is obtained from Equation (8) and is given by,

$$G_{\text{phys}} = \frac{\widehat{U}(k,t+\Delta t)}{\widehat{U}(k,t)} = e^{-\alpha k^2 \Delta t}e^{-ikc\Delta t} \tag{14}$$

The numerical solution of Equation (5) involves knowledge of the following nondimensional parameters, which depend upon the choice of space-time discretization of the governing equation. These are the CFL number (*Nc*) and the diffusion number (*Dn*), corresponding to the physical processes of the convection-diffusion equation. These are expressed as the following:

$$\text{Nc} = \frac{c\Delta t}{h}, Dn = \frac{\alpha \Delta t}{h^2}$$

where h represents the grid spacing, and Δt is the chosen time step. The above non-dimensional parameters are substituted into Equation (14) to obtain the expression for G_{phys} as,

$$G_{\text{phys}} = e^{-Dn(kh)^2} e^{-i(kh)Nc} \tag{15}$$

For this 1D convection-diffusion equation, the numerical dispersion relation can be derived by drawing an analogy with previous studies on pure convection and pure diffusion equations in Sagaut et al. [3] and Sengupta [4]. The numerical dispersion relation is given as:

$$\omega_{\text{num}} = kc_{\text{num}} - i\alpha_{\text{num}}k^2 \tag{16}$$

where c_{num} and α_{num} are the numerical values of the convection speed and diffusion coefficient, respectively. These parameters are not constant during the numerical simulation and are functions of the wavenumber. The numerical amplification factor can readily be determined from the numerical dispersion relation as follows,

$$G_{\text{num}} = e^{-i\omega_{\text{num}}\Delta t} = e^{-\alpha_{\text{num}}k^2\Delta t} e^{-ikc_{\text{num}}\Delta t} \tag{17}$$

The phase shift for each time step Δt can be computed using the relation,

$$\tan(\beta) = -\frac{Im(G_{\text{num}})}{Re(G_{\text{num}})} \Rightarrow \beta = kc_{\text{num}}\Delta t \tag{18}$$

The numerical phase shift for a time step Δt can be computed using the relationship as given in Sagaut et al. [3],

$$\frac{c_{\text{num}}}{c} = \frac{\beta}{kc\Delta t} = -\frac{1}{(kh)Nc}\tan^{-1}\left(\frac{Im(G_{\text{num}})}{Re(G_{\text{num}})}\right) \tag{19}$$

where the ratio c_{num}/c expresses the relationship between the numerical and physical phase speeds.

The numerical group velocity $V_{g,\text{num}}$ can be derived from the numerical dispersion relation by differentiating ω_{num} with respect to k to yield,

$$\frac{V_{g,\text{num}}}{V_{g,\text{phys}}} = \frac{1}{Nc}\frac{d\beta}{d(kh)} \tag{20}$$

where $V_{g,\text{phys}}$ is the physical group velocity for the convection-diffusion equation and is equal to c as given in Sagaut et al. [3].

Finally, the numerical diffusion coefficient α_{num} can be estimated using the numerical amplification factor. From Equation (17), one has the relation $|G_{\text{num}}| = e^{-\alpha_{\text{num}}k^2\Delta t}$, and thus, the numerical diffusion coefficient is given by,

$$\frac{\alpha_{\text{num}}}{\alpha} = -\left(\frac{\ln|G_{\text{num}}|}{Dn(kh)^2}\right) \tag{21}$$

In the presented analysis here, time integration is carried out by the RK_4 scheme that has been used for the NSE also. The NCCD scheme is used for spatial discretization; an enhanced version of the CCD scheme was originally introduced by Chu and Fan [34]. The CCD schemes compute both the first and second-order derivatives simultaneously by using implicit boundary closures. However, due to

numerical instability and attenuation near the inflow and outflow, the NCCD scheme was developed to avoid these issues by using explicit boundary closure schemes in Sengupta et al. [6]. For time integration, the RK_4 can be applied to governing equations as follows: $\frac{\partial u}{\partial t} = L(u)$. The numerical amplification factor G_{num} at a j-th node in the interior of the computational domain can be expressed as in Sengupta et al. [4,35],

$$G_{j,\text{num}} = 1 - A_j + \frac{A_j^2}{2} - \frac{A_j^3}{6} + \frac{A_j^4}{24} \tag{22}$$

where $A_j = -\left[\frac{\Delta t L(\hat{U})}{\hat{U}}\right]_j$.

For the NCCD scheme, the numerical amplification factor $G_{j,\text{num}}$ is evaluated using A_j which is expressed as in Sagaut et al. [3],

$$A_j = Nc \sum_{l=1}^{N} [D_1]_{jl} e^{ik(x_l - x_j)} - Dn \sum_{l=1}^{N} [D_2]_{jl} e^{ik(x_l - x_j)} \tag{23}$$

where $[D_1]$ and $[D_2]$ are formulated as $\{u'\} = \frac{1}{h}[D_1]\{u\}$ and $\{u''\} = \frac{1}{h}[D_2]\{u\}$, where the details of matrices $[D_1]$ and $[D_2]$ are given in Sagaut et al. [3] and Sengupta et al. [6].

Following the procedure from Equations (5)–(23), the *Nc* and *Dn* values are calculated for $\Delta t = 5 \times 10^{-5}$ and $\Delta t = 2 \times 10^{-5}$, with $h = \frac{1}{256}$ for *Re* = 8000, and the $\left|\frac{G_{\text{num}}}{G_{\text{phys}}}\right|$-contours in the (*kh*, *Nc*)-plane are shown plotted for these time steps in **Figures 5** and **6**, respectively.

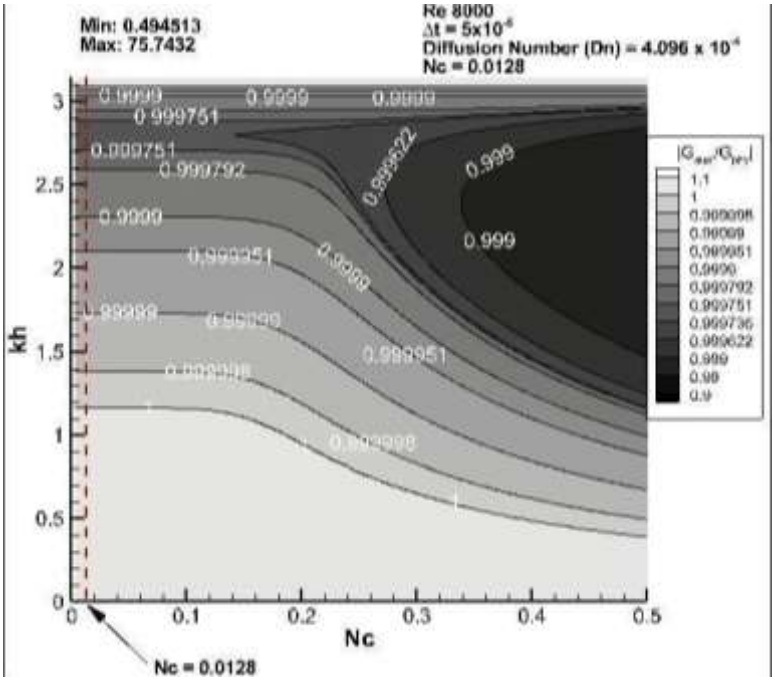

Figure 5. The contours of $|G_{\text{numerical}}/G_{\text{physical}}|$ are shown in the (*kh*, *Nc*)-plane for the time step of $\Delta t = 5 \times 10^{-5}$.

The diffusion number is as indicated, and the operational *Nc* is indicated by the vertical red line in **Figures 5** and **6**.

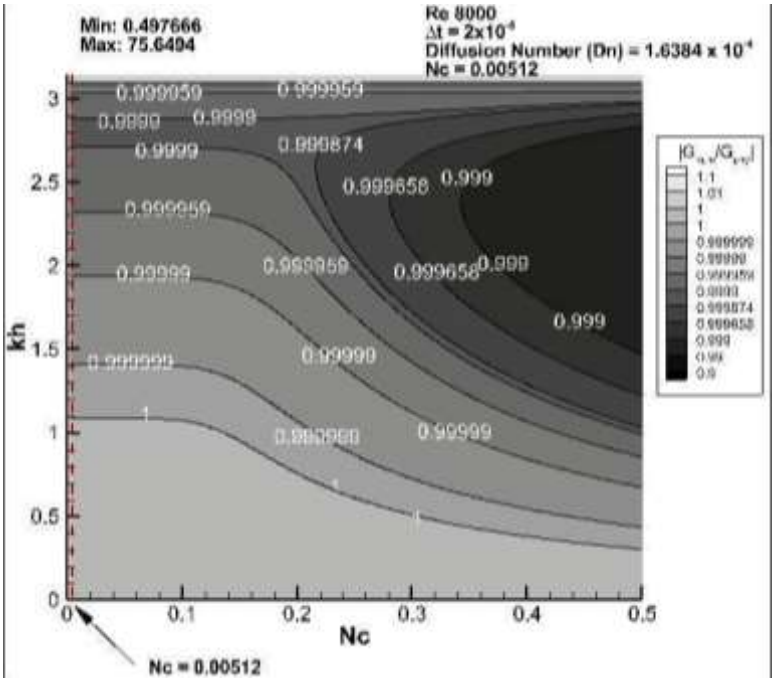

Figure 6. The contours of $|G_{numerical}/G_{physical}|$ are shown in the (*kh*, *Nc*)-plane for the time step of $\Delta t = 2 \times 10^{-5}$.

The *Dn* and the operational *Nc* are as indicated in **Figures 5** and **6**, with the dashed red line represents the *Nc* value for both the time steps and $\left|\frac{G_{\text{num}}}{G_{\text{phys}}}\right|$ values at that operating range of *Nc* for both the time steps that have been shown in **Figure 7**.

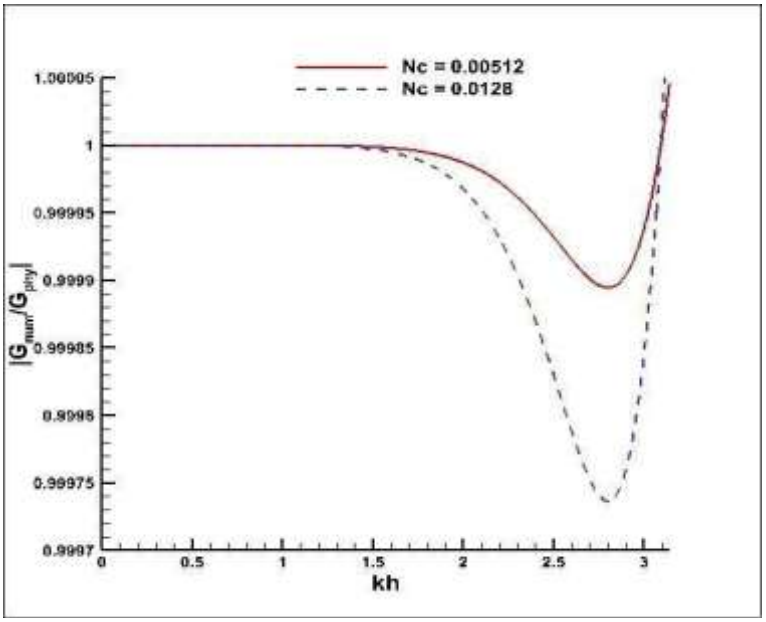

Figure 7. $|G_{numerical}/G_{physical}|$ versus *kh* at the indicated *Nc* = 0.0128 and 0.00512 for the cases of $\Delta t = 5 \times 10^{-5}$ (dashed line) and $\Delta t = 2 \times 10^{-5}$ (solid line).

From **Figure 7**, it is evident that the results for calculated *Nc* = 0.0128 and *Dn* = 4.096×10^{-4} with the time step of $\Delta t = 5 \times 10^{-5}$ show higher attenuation at the higher wavenumbers than for the lower time step of $\Delta t = 2 \times 10^{-5}$ (for which *Nc* and *Dn* values

are 0.00512 and 1.6384×10^{-4}, respectively). This explains the late unsteadiness for the higher time step case and earlier unsteady behavior for the lower time step case, even when the same *Re* flow is computed, as shown in **Figure 4**. Lowering the time step retains the physical disturbance vorticity amplitude without attenuating those at the higher wavenumbers. In contrast, for the higher time step case, those excitations at higher wavenumbers are attenuated, as shown in **Figure 7**. This indicates the flow is diffusion-dominated, with the diffusion number playing the central role as opposed to the commonly held belief about the role of *Nc* for supercritical *Re*.

While the discussion on GSA of the numerical method is presented here using the convection-diffusion equation due to its one-to-one correspondence with the NSE, other investtigations have used GSA for compressible flows by Tan et al. [36], nonlinear waves by Cheviakov et al. [37], and other aspects of the numerical accuracy of the solution of the NSE by Coppola et al. [38,39] and Sjögreen et al. [40].

5. Onset of Instability

The higher magnitude of implicit excitation for LDC flow produced at a lower temporal resolution (as explained with reference to **Figure 7**) causes the flow to show the onset of growth before that for the higher time step case, which is shown in **Figure 8**. From **Figure 8**, it can also be inferred that with a decrease in *Re*, the onset time of linear instability increases asymptotically for $\Delta t = 5 \times 10^{-5}$, and the flow inside the LDC becomes steady below a critical *Re* value, whose exact value is dependent on the grids used and the chosen time step.

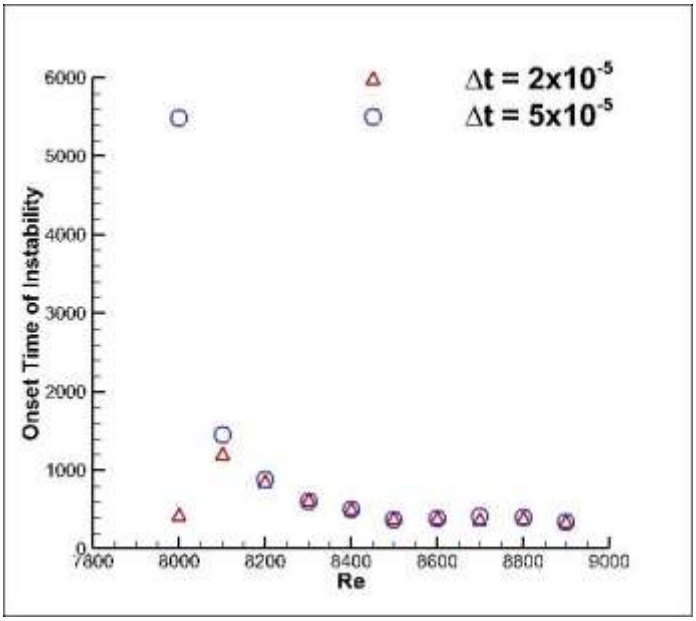

Figure 8. The onset of linear instability for the LDC flow is plotted as a function of *Re.*

It is essential to highlight an aspect of the computed results shown in **Figure 8** for $\Delta t = 2 \times 10^{-5}$ case that has been reported here. In **Figure 2**, one can see the case for $Re = 8500$, where the LDC flow starts off with the display of early violent transients. Subsequently, the transients decay due to physical diffusion. Many vortex-

dominated flows display such transients and are characterized by the presence of multimodal space-time dynamics, as reported in Sengupta et al. [32,41]. Such flows are also referred to as influenced by oscillator-type instability in Chomaz [42].

The results for the LDC flow cases obtained with $\Delta t = 2 \times 10^{-5,}$ which displayed unsteadiness in **Figure 8**, all the computations were started impulsively. The active numerical diffusion allows a larger range of higher wavenumbers to remain less attenuated, as shown and explained for the data in **Figure 7**.

So far, we have noted that LDC flow at higher *Re* is receptive to the background numerical disturbances. Although it is a high *Re* problem, these disturbances at high wavenumbers are amplified due to Gibbs' phenomenon and the growth of aliasing error. Such disturbance growth is attenuated due to numerical diffusion, which is indicated by *Dn*. Following the growth by a linear mechanism, the physical nonlinearity becomes dominant which leads to the formation of the limit cycle about a mean value (ω_m). It has been observed that the increase in *Re* causes an increase in ω_m, as shown in **Figure 9**. This figure also shows that this mean value computed with two different time steps here does not alter the slope of (ω_m versus *Re*)-curve, for both the values of $\Delta t = 5 \times 10^{-5}$ and $\Delta t = 2 \times 10^{-5}$ cases, with the data points falling along the same line.

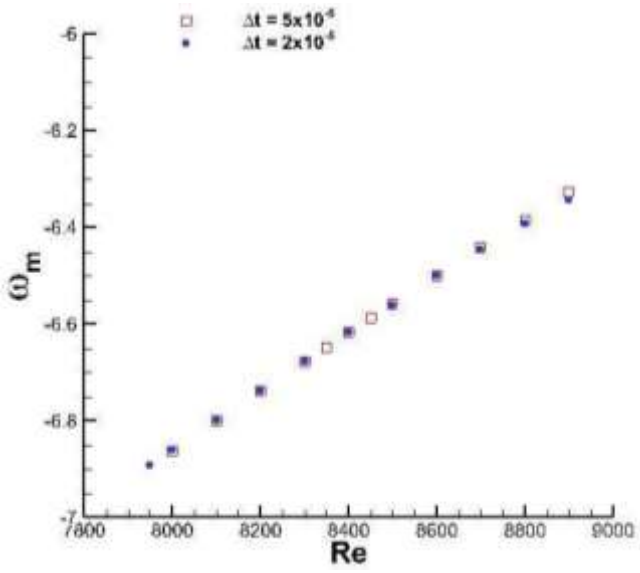

Figure 9. The mean value of vorticity (ω_m) versus *Re* for time steps of $\Delta t = 5 \times 10^{-5}$ and $\Delta t = 2 \times 10^{-5}$.

High-fidelity DNS and it's utility in machine learning

Machine learning (ML) is essentially the process of building models from data using optimization and regression techniques. Because of recent advancements in computational power and data availability, we have much more advanced optimization algorithms, and that's one of the reasons machine learning models like proper orthogonal decomposition (POD), dynamic mode decomposition (DMD), physics-informed neural networks (PINNs) have gained popularity in creating efficient models for studying, optimizing, and controlling complex fluid flows. However, some of these methods rely on high-precision data produced by high-accuracy DNS methods. In

Ranade et al. [17], an ML solver was introduced for solving steady, incompressible NSEs without requiring training data. The solver simultaneously generates and learns solutions for training by approximating PDE residuals using discretization techniques and updated network weights based on the L_2-norm of the residuals.

High-fidelity DNS data is often used to develop reduced order models (ROMs), which retain the critical dynamics of flow while reducing computational costs in Sengupta et al. [43]. ML models introduced in Drakoulas et al. [44] combine ML with singular value decomposition (SVD) to create a Fast SVD-ML-ROM framework for reducing the computational time and forecasting the dynamics of 2D LDC. High-fidelity DNS data informs ML models in medium-range global weather forecasting used in Lam et al. [45]. DNS generates high-resolution flow data that train ML models to reconstruct low-fidelity simulation to DNS-like accuracy in Kochkov et al. [46]. PINNs utilize DNS data to train models that inherently retain flow physics by incorporating the governing equation into the loss function of the neural network. Salim et al. [47] extended PINNs for super-resolution studies of Rayleigh-Benard convection, demonstrating how DNS data helps upscale low-resolution data while preserving physical accuracy. DNS data also enables the development of stabilization techniques like Leray-α models and turbulence closures in numerical simulations, improving the fidelity of ML-enhanced turbulence models as in Pereira et al. [48] and Rogallo [49]. Performing POD of such flows enables one to investigate instability modes involved, visualize their spatial and temporal pictures, and reconstruct the data efficiently Sengupta [29,33] and Sengupta et al. [43].

There were many inconsistencies of results reported as DNS of homogeneous isotropic turbulent flows by the pseudo-spectral method in Rogallo [50] due to the alteration of the governing NSE by adding hyper- and hypo-viscosity terms in Yueng et al. [51], Buaria and Sreenivasan [52], Buaria et al. [53,54] Orszag [55], Gottlieb and Orszag [56]. Ishihara et al. [57,58], Doering and Gibbon [59]. Kraichnan [60] and Batchelor [61]. In Brachet et al. [62], this pseudo-spectral method was used to study the Taylor-Green vortex problem for 2D decaying turbulence, which has been studied in depth and rectified very recently in Sengupta et al. [63]. In recent times, with the advent of high accuracy, HPC of DNS emphasis has shifted from pure DNS of high Reynolds number flows to applications related to ROM and ML, as given in Brunton et al. [25], Jiang et al. [26], Amalinadhi [27], McDevitt et al. [28], Drakoulas et al. [44], Pawar and San [64], Quaini et al. [65], Takhirov et al. [66], Chung et al. [67], Lucor et al. [68], Lam et al. [45], Kochkov et al. [46], Salim et al. [47], Sofos et al. [69], Bastian et al. [49].

6. Summary and conclusion

Some of the principal activities in high-accuracy scientific computing are related to the DNS of canonical instability problems and the DNS of turbulent flows, with and without multiphysics rates of strains in Zhou [70], Zhou et al. [71,72], Joshi et al. [73], Zhou [74], Zhou et al. [75], Pereira et al. [76]. It is worth noting that solving instability problems is more physics-driven, unlike the DNS of turbulent flows, which tends to a nonlinear invariant saturated state. For this reason, an instability problem has been identified for the presented results.

In the present research, the LDC flow has been computed for a supercritical Reynolds number to show the importance of the receptivity to inherent numerical disturbances for a vortex-dominated flow. Computing such flows by high-accuracy methods in Sengupta et al. [6] displays the receptivity aspect graphically, as described in Sengupta [29] due to the properties of the adopted numerical methods.

It is usually understood that such instabilities occurring at high Reynolds numbers would be dominated by the CFL number as in Burggraf [12], Schreiber and Keller [13] for the spatiotemporal growth of the disturbance field, as demonstrated by the bifurcation phenomena described in Landau and Lifshitz [25], Drazin and Reid [30], Ekhaus [31], Sengupta et al. [32]. For the LDC flow, the disturbance growth is shown in **Figure 2**, which shows that following the growth of disturbance vorticity by a linear mechanism, the physical nonlinearity becomes dominant, which leads to the formation of the limit cycle. However, the present state noted in the literature demonstrates the uncertainty about the onset of this bifurcation phenomenon, as indicated for the LDC flow in **Figures 3** and **4**. Note that early researches in Auteri et al. [9] and Sahin and Owens [18] have identified the critical Reynolds number to be above 8000, while the presented results here clearly indicate unsteady flow for Re = 8000, implying the critical Reynolds number to be below Re = 8000. In the present research, with the help of global spectral analysis given in Sengupta et al. [2], Sagaut et al. [3], Sengupta [4] and Sengupta et al. [5], this ambiguity has been explained for the first time by using the model convection-diffusion equation to show the relative importance of the diffusion number as opposed to the CFL number in **Figures 5–7**. These demonstrate the centrality of the numerical diffusion number (Dn) for the LDC. The disturbance growth is due to the presence of omnipresent numerical errors that are highly sensitive to the numerical properties at high wavenumbers due to Gibbs' phenomenon, aliasing, and other sources of errors. As shown in **Figure 7**, taking a higher time step causes attenuation of these high wavenumber error components. The receptivity of the flow to high wavenumber disturbances is determined by the onset of the linear stage of instability to the mean value of vorticity after the nonlinear saturation forming the limit cycle, as indicated in **Figures 8** and **9** for the two time-step cases demonstrated in the present research. We have unsteady solutions for Re = 8000 for both the time steps in **Figure 4**. Thus, the observed results are compatible and as explained with the help of the GSA in **Figures 5** and **6** of the model equations and the HPC of the NSE for many vortex-dominated flows, as in the case of the LDC flow studied here.

In conclusion, the present research achieved the following: (i) By performing DNS of the canonical transitional flow in an LDC, finer physical details are unraveled for the flow following the constraints of disturbance growth as given by the GSA of the related convection-diffusion equation, which captures the convection and diffusion processes of the governing Navier-Stokes equation very accurately; (ii) in simulating LDC flow for two different time steps, it is noted that contrary to the commonly held perception of flow becoming more unsteady with the increase in CFL number (by increasing the time step), this flow captures unsteadiness better with decreased time steps due to reduced attenuation with the diffusion number. Such a behavior of the computed flow field is consistent with the property predicted by GSA; (iii) thus, in various fields of data sciences, such as POD, DMD, ROM, and ML, which require a

very high-fidelity data set for analysis and training, the presented results here for the canonical LDC flow can be used as the benchmark; (iv) specifically, for methods of ML that work like optimizing the data by regression analysis, they can use tools like GSA to convert the same problems as one of constrained optimization, thereby improving the fidelity of the data set.

A direct extension of the present results could continue computing the LDC flow with a smaller time step to capture the critical Reynolds number for the Hopf bifurcation phenomena. Obtained DNS results of the transitional and turbulent flows should be analyzed with tools for the NSE in describing the flows for (a) estimating disturbance growth by mechanical energy, as given in Sengupta [29]; (b) estimating growth by disturbance enstrophy transport equation as given in Sengupta [29]; and (c) tracking coherent vortical structures [77].

Author contributions: Conceptualization, TKS; guide, TKS and AS; formulate research, AP and SKV; results analysis, SKV; post-processing, AP; data curation, AP; writing—original draft preparation, TKS; writing—review and editing, AS; writing—final manuscript, SKV. All authors have read and agreed to the published version of the manuscript.

Acknowledgments: The authors would like to thank Reetesh Ranjan (Univ. of Tennessee, Chattanooga, USA) for useful discussions during the course of the research. At the early stage of this work, Ms. Bhavna Joshi assisted in training the graduate student in computing and post-processing the results. This is gratefully acknowledged.

Conflict of interest: The authors declare no conflict of interest.

References

1. Ghia U, Ghia KN, Shin CT. High-Re solutions for incompressible flow using the Navier-Stokes equations and a multigrid method. Journal of Computational Physics. 1982; 48(3): 387–411. doi: 10.1016/0021-9991(82)90058-4
2. Sengupta S, Sengupta TK, Puttam JK, et al. Global spectral analysis for convection-diffusion-reaction equation in one and two-dimensions: Effects of numerical anti-diffusion and dispersion. Journal of Computational Physics. 2020; 408. doi: 10.1016/j.jcp.2020.109310
3. Sagaut P, Suman VK, Sundaram P, et al. Global spectral analysis: Review of numerical methods. Computers and Fluids. 2023; 261. doi: 10.1016/j.compfluid.2023.105915
4. Sengupta TK. High Accuracy Computing Methods: Fluid Flows and Wave Phenomena. Cambridge University Press; 2013.
5. Sengupta S, Sreejith NA, Mohanamuraly P, et al. Global spectral analysis of the Lax-Wendroff central difference scheme applied to convection-diffusion equation. Computers and Fluids. 2022; 242. doi: 10.1016/j.compfluid.2022.105508
6. Sengupta TK, Lakshmanan V, Vijay VVSN. A new combined stable and dispersion relation preserving compact scheme for non-periodic problems. Journal of Computational Physics. 2009; 228(8). doi: 10.1016/j.jcp.2009.01.003
7. Ozbenli E, Vedula P. Construction of invariant compact finite difference schemes. Physical Review E. 2020; 101. doi: 10.1103/PhysRevE.101.023303
8. Sengupta TK, Ganerwal G, Dipankar A. High accuracy compact schemes and Gibbs' phenomenon. Journal of Scientific Computing. 2004; 21(3). doi: 10.1007/s10915-004-1317-2
9. Auteri F, Quartapelle L, Vigevano L. Accurate ω-ψ spectral solution of the singular driven cavity problem. Journal of Computational Physics. 2002; 180(2): 597–615. doi: 10.1006/jcph.2002.7108
10. Botella O, Peyret R. Benchmark spectral results on the lid-driven cavity flow. Computers and Fluids. 1998; 27(4): 421–433. doi: 10.1016/S0045-7930(98)00002-4

11. Suman VK, Viknesh SS, Tekriwal MK, et al. Grid sensitivity and role of error in computing a lid-driven cavity problem. Physical Review E. 2019; 99(1). doi: 10.1103/PhysRevE.99.013305
12. Burggraf OR. Analytical and numerical studies of the structure of steady separated flows. Journal of Fluid Mechanics. 1966; 24(1): 113–151. doi: 10.1017/S0022112066000545
13. Schreiber R, Keller HB. Driven cavity flows by efficient numerical techniques. Journal of Computational Physics. 1983; 49(2): 310–333. doi: 10.1016/0021-9991(83)90129-8
14. Lestandi L, Bhaumik S, Avatar GRKC, et al. Multiple Hopf bifurcations and flow dynamics inside a 2D singular lid driven cavity. Computers and Fluids. 2018; 166: 86–103. doi: 10.1016/j.compfluid.2018.01.038
15. Sengupta TK, Sundaram P, Suman VK, et al. A high accuracy preserving parallel algorithm for compact schemes for DNS. ACM Transactions on Parallel Computing. 2020; 7(4): 1–32. doi: 10.1145/3418073
16. Sundaram P, Sengupta A, Sengupta TK. A non-overlapping high accuracy parallel subdomain closure for compact scheme: Onset of Rayleigh-Taylor instability by ultrasonic waves. Journal of Computational Physics. 2022; 470. doi: 10.1016/j.jcp.2022.111593
17. Ranade R, Hill C, Pathak J. Discretization Net: A machine-learning based solver for Navier-Stokes equations using finite volume discretization. Computer Methods in Applied Mechanics and Engineering. 2021; 378: 113722. doi: 10.1016/j.cma.2021.113722
18. Sahin M, Owens RG. A novel fully implicit finite volume method applied to the lid-driven cavity problem—Part I: High Reynolds number flow calculations. International Journal for Numerical Methods in Fluids. 2003; 42(1): 57–77. doi: 10.1002/fld.442
19. Bruneau CH, Saad M. The 2D lid-driven cavity problem revisited. Computers and Fluids. 2006; 35(3): 326–348. doi: 10.1016/j.compfluid.2004.12.004
20. Beckers M, van Heijst GJF. The observation of a triangular vortex in a rotating fluid. Fluid Dynamics Research. 1998; 22(5). doi: 10.1016/S0169-5983(97)00039-7
21. Carnevale GF, Kloosterziel RC. Emergence and evolution of triangular vortices. Journal of Fluid Mechanics. 1994; 259: 305–331. doi: 10.1017/S0022112094000157
22. Jansson TRN, Haspang MP, Jensen KH, et al. Polygons on a rotating fluid surface. Physical Review Letters. 2006; 96(17). doi: 10.1103/PhysRevLett.96.174502
23. van der Vorst HA. Bi-CGSTAB: A fast and smoothly converging variant of Bi-CG for the solution of nonsymmetric linear systems. SIAM Journal on Scientific and Statistical Computing. 1992; 13(2). doi: 10.1137/0913035
24. Landau LD, Lifshitz EM. Fluid Mechanics, 2nd ed. Elsevier; 1987.
25. Brunton SL, Noack BR, Komoutsakos P. Machine learning for fluid mechanics. Annual Review of Fluid Mechanics. 2020; 52: 477–508. doi: 10.1146/annurev-fluid-010719-060214
26. Jiang Q, Zhu L, Shu C, et al. Multilayer perceptron neural network activated by adaptive Gaussian radial basis function and its application to predict lid-driven cavity flow. Acta Mechanica Sinica. 2021; 37(12): 1757–1772. doi: 10.1007/s10409-021-01144-5
27. Amalinadhi C, Palar PS, Stevenson R, et al. On physics-informed deep learning for solving Navier-Stokes equations. In: Proceedings of the AIAA SCITECH 2022 Forum; 3–7 January 2022; San Diego, CA, USA.
28. McDevitt C, Fowler E, Roy S. Physics-constrained deep learning of incompressible cavity flow. In: Proceedings of the AIAA SCITECH 2024 Forum; 8–12 January 2024; Orlando, FL, USA.
29. Sengupta TK. Transition to Turbulence: A Dynamical System Approach to Receptivity. Cambridge University Press; UK, 2021
30. Sengupta TK, Vijay VVSN, Singh N. Universal instability modes in internal and external flows. Computers and Fluids. 2011; 40(1): 221–235. doi: 10.1016/j.compfluid.2010.09.006
31. Eckhaus W. Studies in Non-Linear Stability Theory. In: Springer Tracts in Natural Philosophy. Springer; 1965.
32. Drazin PG, Reid WH. Hydrodynamic Stability. Cambridge University Press; 2004.
33. Sengupta TK. Instability of Flows and Transition to Turbulence. CRC Press; 2012
34. Chu PC, Fan C. A three-point combined compact difference scheme. Journal of Computational Physics. 1998; 140(2): 370–399. doi: 10.1006/jcph.1998.5899
35. Sengupta TK, Dipankar A, Sagaut P. Error dynamics: Beyond von Neumann analysis. Journal of Computational Physics. 2007; 226(2): 1211–1218. doi: 10.1016/j.jcp.2007.06.001

36. Tan R, Ooi A, Sandberg RD. Two-dimensional analysis of hybrid spectral/finite difference schemes for linearized compressible Navier-Stokes equations. Journal of Scientific Computing. 2021; 87(42). doi: 10.1007/s10915-021-01442-x
37. Cheviakov AF, Dorodnitsyn V, Kapstov EI. Invariant conservation law-preserving discretizations of linear and nonlinear wave equations. Journal of Mathematical Physics, vol. 61, 081504, 2020, doi: 10.1063/5.0004372
38. Coppola G, Capuano F, de Luca L. Discrete energy-conservation properties in the numerical simulation of the Navier-Stokes equations. Applied Mechanics Review. 2019; 71(1). doi: 10.1115/1.4042820
39. Coppola G, Capuano F, Pirozzoli S, et al. Numerically stable formulations of convective terms for turbulent compressible flows. Journal of Computational Physics. 2019; 382: 86–104. doi: 10.1016/j.jcp.2019.01.007
40. Sjögreen B, Yee HC, Kotov D. Skew-symmetric splitting and stability of high order central schemes. In: Proceedings of the 11th International Conference on Numerical Modeling of Space Plasma Flows: ASTRONUM-2016; 6–10 June 2016; Monterey, CA, USA.
41. Sengupta TK, Singh N, Suman VK. Dynamical system approach to instability of flow past a circular cylinder. Journal of Fluid Mechanics. 2010; 656: 82–115. doi: 10.1017/S0022112010001035
42. Chomaz JM. Global instabilities in spatially developing flows: Non-normality and nonlinearity. Annual Review of Fluid Mechanics. 2005; 37: 357–392. doi: 10.1146/annurev.fluid.37.061903.175810
43. Sengupta TK, Lestandi L, Haider SI, et al. Reduced order model of flows by time-scaling interpolation of DNS data. Advanced Modeling and Simulation in Engineering Sciences. 2018; 5(26). doi: 10.1186/s40323-018-0119-2
44. Drakoulas GI, Goritsas TV, Bourantas GC, et al. Fast SVD-ML-ROM: A reduced order modelling framework based on machine learning for real time application. Computer Methods in Applied Mechanics and Engineering. 2023; 414: 116155. doi: 10.1016/j.cma.2023.116155
45. Lam R, Sanchez-Gonzalez A, Willson M, et al., Learning skillful medium-range global weather forecasting. Science. 2023; 382(6677): 1416–1421. doi: 10.1126/science.adi23
46. Kochkov D, Smith JA, Alieva A, et al., Machine learning-accelerated computational fluid dynamics. PNAS. 2021; 118(21). doi: 10.1073/pnas.2101784118
47. Salim DM, Burkhart B, Sondak D. Extending a physics-informed machine-learning network for superresolution studies of Rayleigh-Benard convection. The Astrophysical Journal. 2024; 964(1). doi: 10.3847/1538-4357/ad1c55
48. Takhirov A, Trenchia C, Waters J. Second order efficient nonlinear filter stabilization for high Reynolds number flows. Numerical Methods for Partial Differential Equations. 2023; 39(1): 90–107. doi: 10.1002/num.22859
49. Bastian P, Altenbernd M, Dreier NA, et al. Exa-Dune-Flexible PDE solvers, numerical methods and applications. Software for Exascale Computing-SPPEXA 2016–2019. Springer; 2020. Volume 136.
50. Rogallo RS. Numerical experiments in homogeneous turbulence. Available online: https://ntrs.nasa.gov/api/citations/19810022965/downloads/19810022965.pdf (accessed on 20 November 2024).
51. Yeung PK, Donzis DA, Sreenivasan KR. Dissipation, enstrophy and pressure statistics in turbulence simulations at high Reynolds numbers. Journal of Fluid Mechanics. 2012; 700: 5–15. doi: 10.1017/jfm.2012.5
52. Buaria D, Sreenivasan KR. Dissipation range of the energy spectrum in high Reynolds number turbulence. Physical Review of Fluids. 2020; 5(9). doi: 10.1103/PhysRevFluids.5.092601
53. Buaria D, Bodenschatz E, Pumir A. Vortex stretching and enstrophy production in high Reynolds number turbulence. Physical Review Fluids. 2020; 5(10). doi: 10.1103/PhysRevFluids.5.104602
54. Buaria D, Pumir A, Bodenschatz E. Self attenuation of extreme events in Navier-Stokes turbulence. Nature Communications. 2020; 11: 5852. doi: 10.1038/s41467-020-19530-1
55. Orszag SA. Numerical methods for the simulation of turbulence. Physics of Fluids. 1969; 12(12). doi: 10.1063/1.1692445
56. Gottlieb D, Orszag SA. Numerical Analysis of Spectral Methods: Theory and Applications. SIAM; 1977.
57. Ishihara T, Gotoh T, Kaneda Y. Study of high-Reynolds number isotropic turbulence by DNS. Annual Review of Fluid Mechanics. 2009; 41: 165–180. doi: 10.1146/annurev.fluid.010908.165203
58. Ishihara T, Morishita K, Yokokawa M, et al. Energy spectrum in high resolution direct numerical simulation of turbulence. Physical Review Fluids. 2016; 1(8). doi: 10.1103/PhysRevFluids.1.082403
59. Doering CR, Gibbon JD. Applied Analysis of the Navier-Stokes Equations. Cambridge University Press; 1995.
60. Kraichnan RH. Inertial range in two-dimensional turbulence. Physics of Fluids. 1967; 10(7): 1417–1423. doi: 10.1063/1.1762301

61. Batchelor GK. Computation of the energy spectrum in homogeneous two-dimensional turbulence. Physics of Fluids. 1969; 12(12): 233–239. doi: 10.1063/1.1692443
62. Brachet ME, Meneguzzi R, Politano H, et al. The dynamics of freely decaying two dimensional turbulence. Journal of Fluid Mechanics. 1988; 194: 333–349. doi: 10.1017/S0022112088003015
63. Sengupta TK, Sarkar A, Joshi B, et al. Direct simulation of vortex dynamics of multicellular Taylor-Green vortex by Pseudospectral method. European Journal of Mechanics/B Fluids. 2024; 108: 226–236. doi: 10.1016/j.euromechflu.2024.08.004
64. Pawar S, San O. Equation free surrogate modelling and geophysical flows at the intersection of machine learning and data assimilation. Journal of Advanced Modelling Earth System. 2022; 14(11). doi: 10.1029/2022MS003170
65. Quaini A, San O, Veneziani A, et al. Bridging large eddy simulation and reduced order modelling of convection dominated flows through spatial filtering: Reviews and perspectives. Fluids. 2024; 9(8): 178. doi: 10.3390/fluids9080178
66. Takhirov A, Trenchia C. Efficient nonlinear filter stabilization of the Leray-α model. Journal of Computational Physics. 2022; 471: 111668. doi: 10.1016/j.jcp.2022.111668
67. Chung WT, Jung KS, Chen JH, et al. BLASTNet: A call for community-involved big data in combustion machine learning. Applications in Energy and Combustion Science. 2022; 12: 100087. doi: 10.1016/j.jaecs.2022.100087
68. Lucor D, Agrawal A, Sergeant A. Simple computational strategies for more effective physics informed neural networks modeling of turbulent natural convection. Journal of Computational Physics. 2022; 456: 111022. doi: 10.1016/j.jcp.2022.111022
69. Sofos F, Drikakis D, Kokkinakis IW, et al. A deep learning super-resolution model for turbulent image upscaling and its application to shock wave-boundary layer interaction. Physics of Fluids. 2024; 36(2). doi: 10.1063/5.0190272
70. Zhou Y. Turbulence theories and statistical closure approaches. Physics Report. 2021; 935: 1–117. doi: 10.1016/j.physrep.2021.07.001
71. Zhou Y, Clark TT, Clark DS, et al. Turbulent mixing and transition criteria of flows induced by hydrodynamic instabilities. Physics of Plasmas. 2019; 26(8). doi: 10.1063/1.5088745
72. Zhou Y, Williams RJR, Ramaprabhu P, et al. Rayleigh-Taylor and Richtmeyer-Meshkov instabilities: A journey through peaks. Physica D: Nonlinear Phenomena. 2021; 423. doi: 10.1016/j.physd.2020.132832
73. Joshi B, Sengupta TK, Sundaram P, et al. Highly resolved Peta-scale DNS: Onset of Kelvin-Helmholtz Rayleigh-Taylor instability via pressure pulses. Computers and Fluids. 2024; 284: 106442. doi: 10.1016/j.compfluid.2024.106442
74. Zhou Y. Hydrodynamic Instabilities and Turbulence: Rayleigh-Taylor, Richtmeyer-Meshkov and Kelvin-Helmholtz Mixing. Cambridge University Press; 2024.
75. Zhou Y, Saddler JD, Hurricane OA. Instabilities and mixing in inertial confinement fusion. Annual Review of Fluid Mechanics. 2025; 57: 197–225. doi: 10.1146/annurev-fluid-022824-110008
76. Pereira FS, Grinstein FF, Israel D. Effect of numerical discretization schemes in shock driven turbulent mixing simulations. Computers and Fluids. 2020; 201: 104487. doi: 10.1016/j.compfluid.2020.104487
77. Sengupta TK, Sharma PK, Sengupta A, et al. Tracking disturbances in transitional and turbulent flows: Coherent structures. Physics of Fluids. 2029; 31(12): 124106. doi: 10.1063/1.5130918